metals

MDPI

Article

Numerical Simulation of Tundish Filter Geometry: Effects of Pore Number and Elevation Angle on Inclusion Removal in Molten Steel

Aiwei Lv [1], Dong Feng [1,*], Xudong Luo [1,*], Siyao Liu [1], Jiegang You [1] and Dabin Qi [2]

[1] School of Materials and Metallurgy, University of Science and Technology Liaoning, Anshan 114051, China; yebinglee@163.com (A.L.)
[2] School of Computer Science and Software Engineering, University of Science and Technology Liaoning, Anshan 114051, China
* Correspondence: fengdong_neu@163.com (D.F.); luoxudong@aliyun.com (X.L.)

Abstract

To improve steel cleanliness during continuous casting, tundish flow-control devices must effectively regulate molten-steel flow and promote the removal of non-metallic inclusions. In this study, a numerical investigation was conducted to clarify the coupled effects of pore number and pore elevation angle in an inclined porous tundish filter on molten-steel flow behavior and inclusion removal. Twenty-five filter configurations were compared by varying the pore number from 2 to 32 pores and the pore elevation angle from 20° to 40° while maintaining an identical total flow-through area. The results show that inclusion removal is governed by the combined effects of flow guidance, velocity-field uniformity, and post-filter streamline distribution, with the filter containing 8 pores and a 40° pore elevation angle achieving the highest average inclusion removal efficiency of 74.33% for 20–80 μm inclusions. These findings provide a quantitative basis for optimizing tundish filter geometry and improving steel cleanliness during continuous casting.

Keywords: tundish filter; non-metallic inclusion; inclusion removal efficiency; pore number; pore elevation angle; flow-field distribution

1. Introduction

To meet the escalating demand for high performance steel in advanced equipment manufacturing, the metallurgical industry has imposed increasingly stringent control standards on steel cleanliness. This has driven the evolution of the tundish from a simple molten-steel distributor to a core reaction unit with refining capabilities [1,2]. As the critical buffer linking the ladle and mold in continuous casting, modern tundish systems undertake the dual functions of regulating steel-temperature distribution and promoting non-metallic inclusion removal. Their efficiency directly determines the microstructure and mechanical properties of cast billets [3]. Consequently, improving molten-steel cleanliness at the tundish stage has become a pivotal industry challenge. Figure 1 compares the conventional tundish equipped with weirs and dams and the proposed tundish with an inclined porous filter.

During steel continuous casting, the tundish serves as the final metallurgical reactor before solidification, where cleanliness control decisively influences final product quality. Residual non-metallic inclusions, particularly micron-sized Al_2O_3, calcium aluminates, and magnesia-alumina spinel, not only disrupt matrix continuity but also induce fatigue

Check for updates

Academic Editor: Noé Cheung

Received: 27 April 2026
Revised: 19 May 2026
Accepted: 22 May 2026
Published: 23 May 2026

Copyright: © 2026 by the authors. Licensee MDPI, Basel, Switzerland. This article is an open access article distributed under the terms and conditions of the Creative Commons Attribution (CC BY) license.

cracks, degrade mechanical properties, and reduce corrosion resistance. This poses severe challenges for producing high-grade specialty steels [4,5]. To optimize inclusion removal kinetics, multistage flow-control devices are widely deployed in tundishes: weirs and dams constitute fundamental passive flow-control devices [6,7]. The weir extends the molten-steel flow path through vertical obstruction, facilitating the flotation of large inclusions, whereas the dam alters the flow direction via a horizontal barrier and creates a low-turbulence zone behind it. This reduces vortex-induced slag entrainment and establishes quiescent conditions for inclusion flotation and removal. Industrial practice demonstrates that optimized weir dam configurations can reduce tundish dead volume below 15%, extend average residence time by 30–40%, and significantly enhance removal efficiencies for inclusions > 50 μm [8,9]. However, conventional weir dam systems face inherent physical limitations in capturing inclusions within the critical size range (from 20 to 50 μm) [10]. Such inclusions exhibit slow flotation velocities and tend to remain suspended due to turbulent diffusion, struggling to reach the steel–slag interface within limited residence times [11,12]. To address this limitation, filter-based flow-control technologies, such as permeable ceramic filters, multi-hole baffles, and straight-through channel structures, have been introduced into tundish metallurgy systems [13,14]. Zhao et al. comparatively investigated molten-steel flow characteristics in a two-strand slab continuous casting tundish equipped with conventional slag dams and filter-type flow-control devices by combining numerical and physical simulations. Their results demonstrated that filter channels could improve inclusion interception and enhance slab cleanliness [15]. Jin et al. studied the effects of a 30° inclined double-layer porous baffle on tundish flow behavior, residence time, and inclusion removal using numerical and physical simulation methods. They reported that, under an inlet velocity of 1.02 m/s at the submerged entry nozzle, the inclined porous baffle optimized internal flow-field distribution, prolonged the average residence time of molten steel, and improved the removal efficiency of fine inclusions [16].

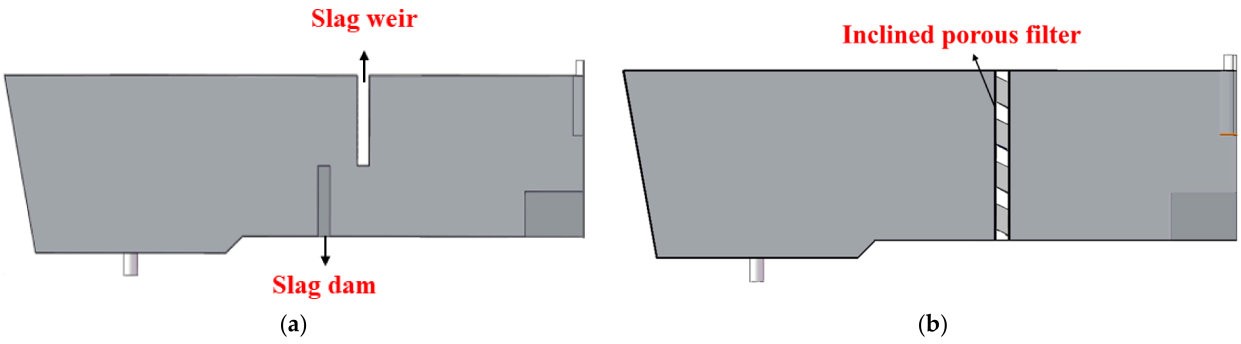


Figure 1. Comparison between the conventional tundish and the proposed tundish model: (**a**) conventional tundish with weirs and dams; (**b**) proposed tundish with an inclined porous filter.

Compared with conventional weirs and dams, tundish filters act not only as flow-control devices but also as potential inclusion-capture media. When molten steel passes through filter channels, the pore geometry redistributes the local velocity field, modifies the streamline pattern, and changes the migration trajectory of non-metallic inclusions [17,18]. These effects can suppress short-circuiting flow, prolong the effective residence time of molten steel, and increase the probability of inclusions migrating toward the slag/flux layer or being intercepted by filter surfaces [19,20]. Therefore, the metallurgical performance of a tundish filter is strongly dependent on its geometric parameters, including pore number, pore size, total flow-through area, channel orientation, and spatial arrangement [21,22].

However, the relationship between filter geometry and inclusion removal remains complex. A small number of pores may produce localized high-velocity jets, leading to nonuniform flow distribution and limited effective filtration area [23]. By contrast, excessive

pore number may cause flow dispersion and weaken the directional transport of inclusions toward the upper region of the tundish. Moreover, inclined or elevated filter channels can guide molten steel upward and enhance inclusion flotation, but the optimal pore elevation angle is closely coupled with pore number and inclusion size [24,25]. To date, most studies have focused on a single-filter structure or a fixed inclination angle, while the combined effects of pore number and pore elevation angle on flow-field evolution and inclusion removal across different particle sizes remain insufficiently clarified [26].

Based on the above considerations, this study develops a tundish filter with inclined pore channels and systematically investigates the coupled effects of pore number and pore elevation angle on molten-steel flow behavior and non-metallic inclusion removal. Five pore-number configurations, namely 2, 4, 8, 16, and 32 pores, and five pore elevation angles, namely 20°, 25°, 30°, 35°, and 40°, were evaluated while maintaining an identical total flow-through area. The discrete phase model was employed to track Al_2O_3 inclusions with diameters of 20–80 μm, and the corresponding velocity field, streamline distribution, vector distribution, and inclusion removal efficiency were quantitatively analyzed. The objective of this work is to clarify the pore-number/pore-elevation-angle coupling mechanism and provide a quantitative basis for optimizing tundish filter design for cleaner continuous casting.

2. Model Description and Methodology

2.1. Mathematical Modelling

A three-dimensional numerical model was established to investigate the effects of tundish filter structural parameters on molten-steel flow behavior and non-metallic inclusion removal. In this study, two key geometric variables were considered: pore number and pore elevation angle. Five pore-number configurations, namely 2, 4, 8, 16, and 32 pores, and five pore elevation angles, namely 20°, 25°, 30°, 35°, and 40°, were selected. Accordingly, a full-factorial simulation matrix containing 25 cases was constructed to clarify the coupled influence of pore number and pore elevation angle on flow-field evolution and inclusion removal efficiency.

To ensure the comparability of different filter configurations, the total flow-through area of each filter was kept identical and equivalent to the flow passage area of the conventional dam structure. Therefore, the variation in flow behavior among different cases was mainly attributed to pore number, pore spatial distribution, and pore elevation angle rather than to changes in the total open area. The pores were arranged symmetrically with respect to the central axis of the filter to maintain a balanced flow distribution on both sides of the tundish.

In the present study, pore number and pore elevation angle were treated as design variables in a comparative parametric analysis, while all other boundary conditions were unchanged. The selected pore numbers of 2, 4, 8, 16, and 32 pores were used to represent low-, intermediate-, and high-pore-number configurations. The pore-elevation-angle range of 20–40° was determined according to the geometric feasibility of the filter structure. Under the constraint of constant total flow-through area, pore elevation angles greater than 40° would make it difficult to arrange the inclined channels completely within the filter body. Therefore, 40° was taken as the upper limit in the present study.

For the pore arrangement, a graded nonuniform distribution strategy was adopted. The filter cross-section was divided into several characteristic regions according to the upper, lower, and lateral reference positions of the filter plate. In the low-pore-number configurations, the pores were preferentially arranged in a symmetric upper–lower pattern to guide the main molten-steel stream while avoiding severe flow bias. With increasing pore number, additional pores were gradually distributed toward the lateral and intermediate

regions according to the local cross-sectional area, so that the effective flow channels covered the filter section more uniformly. This arrangement prevented excessive concentration of pores in the central region and reduced the risk of localized high-velocity jets, while maintaining comparable overall permeability among different pore-number configurations.

The pore elevation angle was introduced as the main directional-control parameter of the filter channels. By inclining the channels upward, the molten steel passing through the filter could be guided toward the upper region of the tundish, thereby increasing the probability of inclusion migration toward the slag/flux layer and filter surfaces. The pore elevation angle was therefore expected to affect both the residence behavior of molten steel and the transport trajectory of inclusions. Based on the geometric symmetry of the tundish, only one half of the tundish was modeled to reduce computational cost. The single-side three-dimensional model used for the numerical simulation is shown in Figure 2.

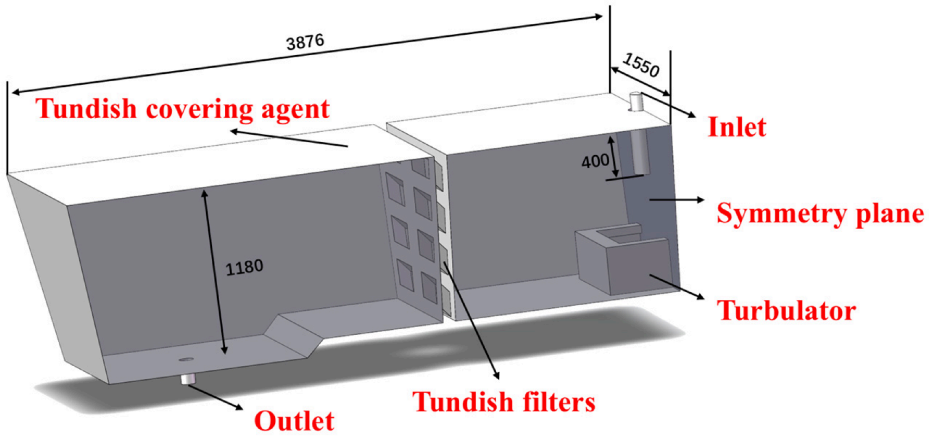


Figure 2. Three-dimensional model of developed tundish with pore elevation angle filter.

The computational domain consisted of the tundish wall, ladle shroud, submerged entry nozzle, turbulence inhibitor, and porous filter. Filters with 2, 4, 8, 16, and 32 pores were established, respectively. In the half-tundish model, the length and width at the top molten-steel level were 3876 mm and 1550 mm, respectively. The inner diameters of the ladle shroud and submerged entry nozzle were 120 mm and 90 mm, respectively. The molten-steel bath height was 1180 mm, and the immersion depth of the submerged entry nozzle was 400 mm. The cross-sectional pore arrangements of different filter configurations are shown in Figure 3.



Figure 3. Cross-sectional views of the tundish filter showing pore arrangements: (**a**) 2 pores, (**b**) 4 pores, (**c**) 8 pores, (**d**) 16 pores, and (**e**) 32 pores.

2.2. Filter Design

This study innovatively replaces traditional tundish dams and weirs with porous filters, optimizing molten-steel flow characteristics through specifically designed pore elevation angles. Based on fluid dynamics principles, the tundish is divided into two functional zones (Zone A and Zone B): Zone A refers to the flow region from molten steel entry

into the tundish to the filter section, while Zone B encompasses the molten-steel movement area downstream of the filter to the outlet, as illustrated in Figure 4.

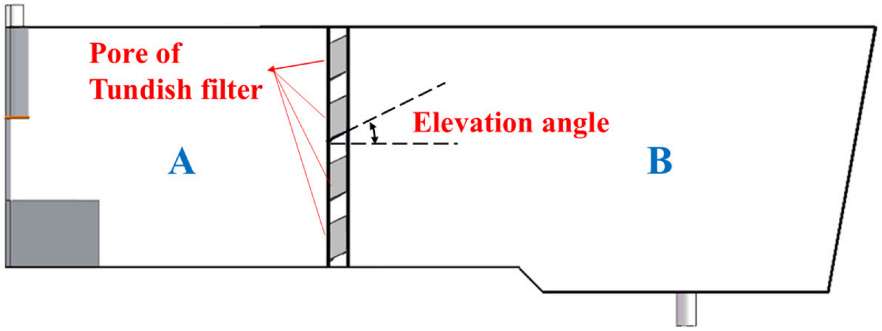


Figure 4. The right side of the tundish, including area A and area B.

Based on the geometric proportional relationship of traditional tundish dam and bottom structures, theoretical calculations determined that the molten-steel flow passage occupies 36% of the tundish cross-sectional area. To isolate the effect of filter channel inclination, the total porosity of the porous filter was kept constant, while the pore elevation angles of the filter channels were set to 20°, 25°, 30°, 35°, and 40°, respectively. Using numerical simulation methods, this study systematically investigates the effects of pore-number and pore-elevation-angle variations on molten-steel flow-field distribution characteristics and non-metallic inclusion removal efficiency.

2.3. Governing Equations and Numerical Methods

The numerical simulation in this study was carried out using ANSYS Workbench 2021 R2 with ANSYS Fluent as the solver. The pressure–velocity coupling was handled using the SIMPLE algorithm. The flow field was initialized using the standard initialization method in ANSYS Fluent. The absolute residual convergence criterion for the iterative solution was set to 1.0×10^{-6}, and the monitored flow-field variables were also checked to ensure that the solution reached a stable state before post-processing. This study employs the standard k-epsilon turbulence model, which demonstrates significant engineering applicability in simulating molten-steel flow within tundishes [27]. Since the inlet velocity, molten-steel properties, and total flow-through area were kept constant for all simulated cases, the flow in the tundish remained within a high-Reynolds-number turbulent regime, although the local velocity distribution changed with pore number and pore elevation angle. Therefore, the standard k–ε turbulence model was considered appropriate for all configurations studied in this work. By solving transport equations for turbulent kinetic energy (k) and its dissipation rate (ε), this model efficiently captures the isotropic turbulence characteristics of molten steel under a high Reynolds number, providing a reliable flow field foundation for inclusions transport calculations. Its thoroughly validated stability and lower computational cost make it particularly suitable for systematic batch simulations of multiparameter combination conditions, enabling a quantitative analysis of how filter-structure variations affect local vortex scales and turbulent kinetic energy distribution. Consequently, it provides a reliable basis for predicting the migration trajectories and removal behavior of inclusions with different sizes within complex tundish flow fields, ensuring reasonable accuracy in the calculation of inclusion removal efficiency.

Given the geometric symmetry of the continuous casting tundish, the vessel was divided equally at the inlet, with numerical simulations performed only on molten steel within this half region. The molten steel was treated as an incompressible viscous fluid exhibiting single-phase steady-state turbulent flow. Inclusion particles were simplified as spheres, and interparticle collisions, aggregation, and growth were not considered.

The tundish flux cover was assumed not to affect the flow-field distribution, but it was considered to capture inclusions reaching the steel surface. In addition, the present simulation was conducted under isothermal conditions, and heat transfer between molten steel and the filter was not considered. These assumptions simplify the numerical model and improve computational efficiency, but they may influence the quantitative prediction of local flow details and inclusion transport behavior. Therefore, the present study should be understood as a comparative parametric analysis of pore number and pore elevation angle under controlled numerical conditions rather than a complete representation of all physical phenomena in industrial tundish operation.

Molten-steel flow within the tundish employs the standard k–ε model. In this simulation, the steady-state flow of the molten-steel phase follows the continuity equation, momentum equation (Navier–Stokes equations), and inclusions motion equation.

$$\frac{\partial \rho}{\partial t} + \frac{\partial (\rho_{v_x})}{\partial x} + \frac{\partial \left(\rho_{v_y}\right)}{\partial y} + \frac{\partial (\rho_{v_z})}{\partial z} = 0 \tag{1}$$

where ρ is the molten-steel density $\left(\mathrm{kg/m^3}\right)$; t is the flow time (s); x, y, and z are the three-dimensional coordinates (m); and v_x, v_y, and v_z denote the velocity components of molten steel in the x-, y-, and z-directions $(\mathrm{m/s})$, respectively.

$$\frac{\partial (\rho u_j\, u_i)}{\partial x_j} = -\frac{\partial P}{\partial x_i} + \frac{\partial}{\partial x_j}\left(u_{eff}\frac{\partial u_i}{\partial x_j}\right) + \frac{\partial}{\partial x_j}\left(u_{eff}\frac{\partial u_j}{\partial x_i}\right) + \rho g_i \tag{2}$$

where u_i and u_j are the time-averaged velocity components of molten steel in the i and j directions $(\mathrm{m/s})$, respectively; x_i and x_j are the coordinate directions (m); P is the pressure (Pa); μ_{eff} is the effective viscosity $(\mathrm{Pa \cdot s})$; and g_i is the gravitational acceleration component $\left(\mathrm{m/s^2}\right)$.

The discrete phase model (DPM) was used to simulate the trajectories of inclusions in molten steel within the tundish. In molten steel, inclusions are subjected to gravity, buoyancy, drag force, Saffman lift force, and pressure-gradient force. In the simulation, alumina inclusions were assumed to have a density of 3970 $\mathrm{kg/m^3}$, and the inclusion diameters were set as 20, 30, 40, 50, 60, 70, and 80 μm. The governing equations for inclusion motion are expressed as follows:

$$\frac{du_p}{dt} = F_D(u - u_p) + \frac{g(\rho_p - \rho)}{\rho_p} + F_x \tag{3}$$

$$F_D = \frac{18\mu}{\rho_p d_p^2}.\frac{C_D \cdot Re}{24} \tag{4}$$

where F_D is the drag term coefficient $\left(\mathrm{s^{-1}}\right)$; u is the molten-steel velocity $(\mathrm{m/s})$; u_p is the inclusion-particle velocity $(\mathrm{m/s})$; ρ is the molten-steel density $\left(\mathrm{kg/m^3}\right)$; ρ_p is the particle density $\left(\mathrm{kg/m^3}\right)$; d_p is the inclusion-particle diameter (m); C_D is the drag coefficient; Re is the particle Reynolds number; F_x represents other additional force terms per unit particle mass $\left(\mathrm{m/s^2}\right)$; g is the gravitational acceleration $\left(\mathrm{m/s^2}\right)$; t is time (s); and μ is the dynamic viscosity of molten steel $(\mathrm{kg/(m \cdot s)})$.

F_x represents the resultant additional force term, other than the drag and gravity-buoyancy terms, including virtual mass force, Saffman lift force, and pressure-gradient force. Gravity and buoyancy are both vertical forces, with gravity acting downward and buoyancy acting upward. Figure 5 shows the force-analysis schematic diagram of inclusion motion in molten steel.

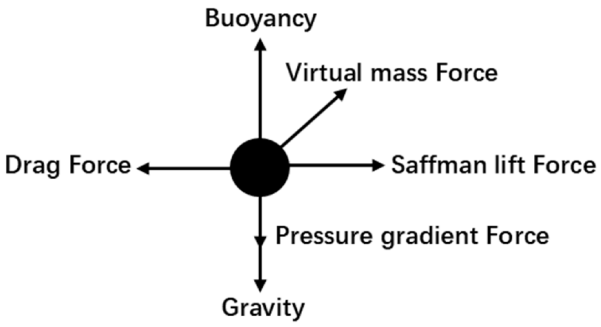


Figure 5. Force analysis schematic diagram of inclusion movement in molten steel.

2.4. Boundary Condition

Based on the slab cross-sectional dimensions (1.5 m × 0.6 m) and average casting speed (1.5 m/min), the molten-steel velocity at the tundish inlet is calculated as 1.33 m/s. The steel-flow direction follows the ladle-shroud axial distribution. The numerical simulation implemented the following boundary conditions: the outlet boundary adopted free outflow conditions to ensure flow continuity, and the inlet boundary was defined as a velocity inlet, with non-metallic inclusions uniformly distributed across the inlet cross-section at the same initial velocity as molten steel. For all simulated cases, the same inclusion-injection condition was adopted, and the inclusion removal efficiency was defined as the ratio of captured inclusions to the total inclusions introduced at the inlet. The top wall was set as a capture boundary where inclusions reaching the steel surface were considered captured by the flux cover; solid walls (including tundish perimeter walls, bottom, turbulence inhibitor, and baffle surfaces) employed reflective boundaries to simulate elastic collision behavior between inclusions and refractory materials; all porous media surfaces at the filter interface were designated capture boundaries to characterize the adsorption interception mechanism; and the outlet condition was defined as an escape boundary where inclusions arriving at this zone were deemed to have entered the mold. The physical properties used in the simulation were as follows: molten-steel density 7020 kg/m^3, dynamic viscosity 0.0062 kg/m·s, inclusion density 3970 kg/m^3, and inclusion diameters of 20, 30, 40, 50, 60, 70, and 80 μm.

2.5. Meshing

The computational domain was discretized using an unstructured tetrahedral mesh due to the complex geometries of the tundish, turbulence inhibitor, and inclined filter channels. Local mesh refinement was applied near the inlet, outlet, turbulence inhibitor, filter channels, and solid-wall boundaries, where relatively large velocity gradients were expected. The characteristic mesh sizes were set to 0.005 m in the inlet and outlet regions, 0.01 m near the turbulence inhibitor and filter, and 0.02 m in the main flow region. Prism layers were generated near solid walls to improve the resolution of near-wall flow gradients.

To evaluate mesh independence, three mesh schemes were tested: a coarse mesh with approximately 0.8 million cells, a medium mesh with approximately 1.5 million cells, and a fine mesh with approximately 2.3 million cells. Mesh sensitivity was assessed by comparing the velocity-field distribution and inclusion removal efficiency under the representative filter configuration. The results showed that the difference between the medium and fine meshes was less than 1% for the main evaluated parameters. Therefore, the medium mesh was selected for the subsequent simulations to balance numerical accuracy and computational cost. The topology of the medium-resolution mesh adopted for the subsequent simulations is shown in Figure 6.

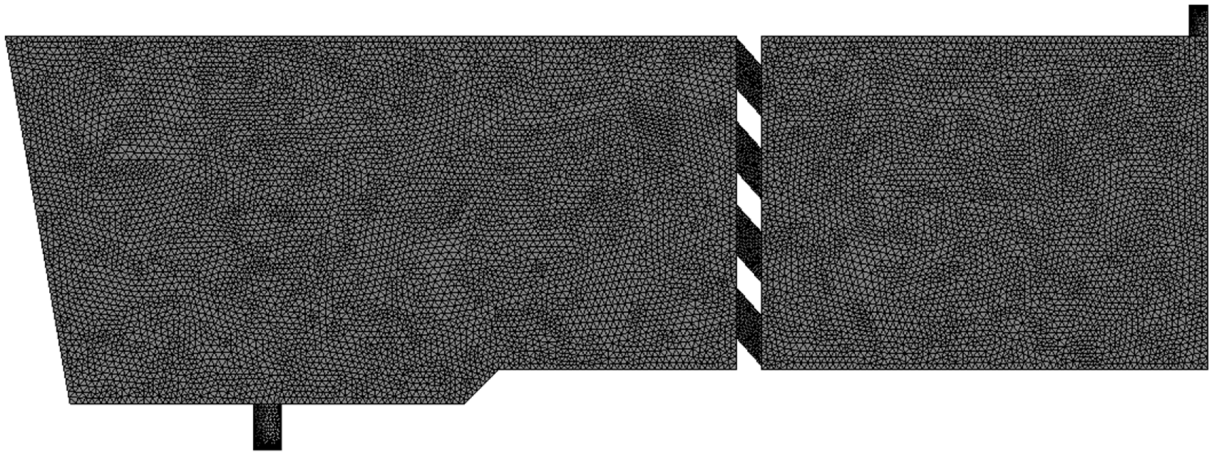


Figure 6. Topology of the medium-resolution mesh adopted for the subsequent simulations.

3. Results and Discussion

3.1. Influence of Pore Number and Pore Elevation Angle of the Filter on the Inclusion Removal Efficiency of Molten Steel in the Tundish

Figure 7 illustrates the relationship between varying tilt angles of multi-pore tundish filters and the average removal efficiency of different-sized inclusions (particle size range: 20 μm to 80 μm) in molten steel, with an inlet velocity set to 1.33 m/s. Specific numerical values are presented in Table 1. Figure 7 reveals that as the pore elevation angle of tundish filters with varying pore counts changes from 20° to 40°, the removal efficiency consistently exhibits a fluctuating curve trend. This manifests as patterns of initial increase followed by a decrease and subsequent rise or initial decrease followed by an increase. During angular variations of filters with different pore numbers, "relative minima" in removal efficiency occur at specific angles. Notably, the 4-pore filter demonstrates its lowest removal efficiency at 25° elevation, with a value of 65.00%. Most filter configurations reach their highest removal efficiency at 40° elevation, except for the 32-pore filter, which shows its peak value of 73.69% at 30°. Among all cases, the 8-pore filter at 40° achieves the highest average inclusion removal efficiency of 74.33%. The results also indicate a clear interaction effect between pore number and pore elevation angle on inclusion removal efficiency. The influence of pore elevation angle is not identical for all pore-number configurations. For the 2-pore and 4-pore filters, the variation in removal efficiency with increasing elevation angle is relatively limited. By contrast, the 8-pore and 16-pore filters show a more pronounced improvement in inclusion removal efficiency as the pore elevation angle increases. The 32-pore filter exhibits a different response, with its highest removal efficiency occurring at 30° rather than 40°. These results suggest that the effect of elevation angle depends strongly on pore number, and that the optimal filter configuration is determined by the coupled action of these two structural parameters rather than by either parameter alone. When molten steel flows directly through the filters, different pore configurations alter the tundish flow field, indicating that removal efficiency undergoes significant variations corresponding to changes in filter pore number and pore elevation angle.

The results indicate that inclusion removal is governed by the coupled effects of pore number, pore elevation angle, and inclusion size. Among the tested configurations, the filter with 8 pores and a 40° pore elevation angle achieve the highest average removal efficiency of 74.33% for inclusions in the size range of 20–80 μm. This result suggests that a moderate pore number can improve flow-field uniformity and inclusion transport while avoiding excessive flow concentration or dispersion.

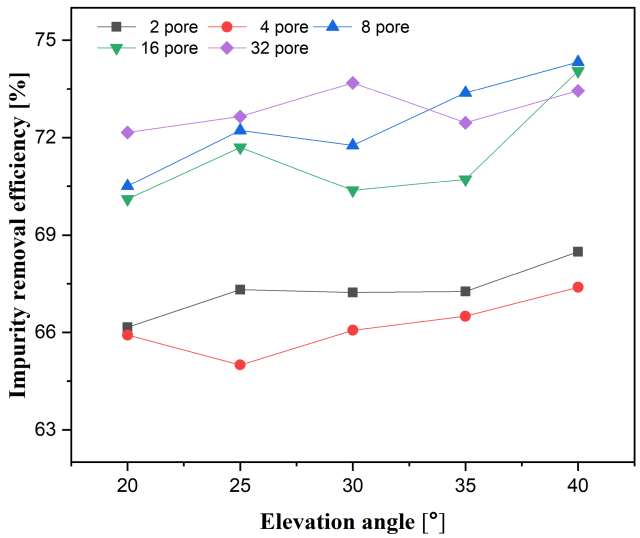


Figure 7. The relationship between filter pore elevation angle/pore number and inclusion removal efficiency in molten steel.

Table 1. Effect of pore number and pore elevation angle on the average inclusion removal efficiency of molten steel.

Pore Number	Pore Elevation Angle [°]				
	20	**25**	**30**	**35**	**40**
2 pores	66.16	67.32	67.23	67.26	68.49
4 pores	65.92	65.00	66.07	66.50	67.39
8 pores	70.51	72.22	71.76	73.38	**74.33**
16 pores	70.11	71.70	70.38	70.72	74.05
32 pores	72.16	72.65	73.69	72.46	73.44

Note: Values represent the average inclusion removal efficiency (%). The bold value indicates the highest removal efficiency among all filter configurations.

As shown in Figure 8, angle regulation of filtration performance exhibits significant size-dependent effects: when the pore elevation angle increases from 20° to 40°, the removal efficiency rises by 6.2% on average for large inclusions (>50 μm) versus 8.5% for small particles (20–40 μm). High pore elevation angles (>35°) enhance gravity-driven segregation, promoting inclusion enrichment toward filter surfaces. However, a threshold effect exists regarding pore number when the pore number exceeds 16 pores: flow-field uniformity decreases, intensifying efficiency fluctuations for sub-50 μm inclusions (e.g., 20 μm removal at 32 pores and 40° decreases by 4.7% versus the 8-pore configuration). Additionally, the 32-pore and 30° configuration shows an anomalous peak (73.69%) in 50 μm inclusion removal. Flow-field analysis suggests this may originate from transient micro vortices enhancing capture probability, although such flow instabilities may induce slag-entrainment risks during prolonged operation.

Studies indicate that inclusion removal efficiency exhibits significant particle-size dependence, consistently increasing with larger inclusion size across all five pore configurations. The 8-pore filter demonstrates superior comprehensive filtration performance, achieving 64.03% removal efficiency for 20 μm fine inclusions and 89.08% for 80 μm large particles, both representing the highest values among all configurations. This phenomenon suggests that moderate pore density ensures sufficient contact area while effectively preventing turbulence intensification caused by excessively dense pores, thereby enabling efficient collaborative removal of inclusions across different sizes.

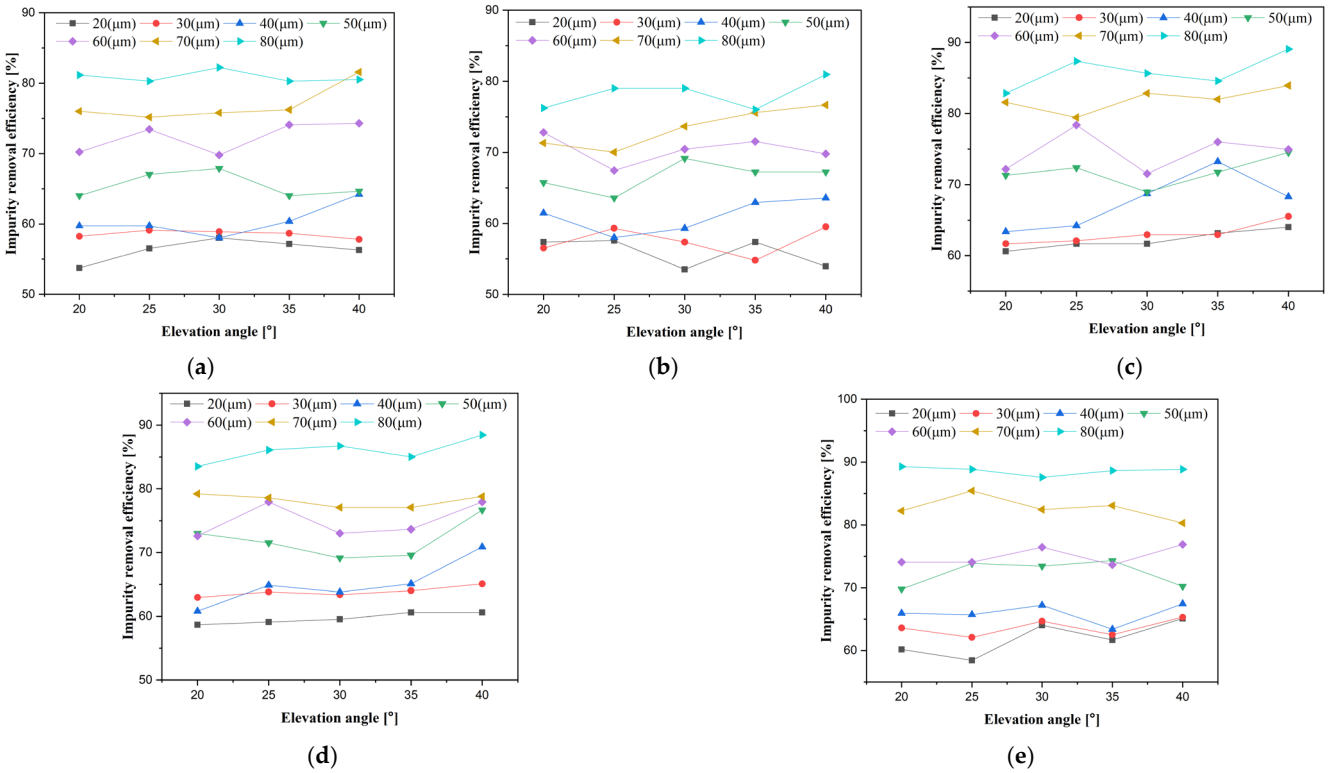


Figure 8. The influence of the filter pore number and the size of inclusions on the inclusion removal efficiency of molten steel: (**a**) 2 pores, (**b**) 4 pores, (**c**) 8 pores, (**d**) 16 pores, (**e**) 32 pores.

Further analysis reveals that when the pore number increases to 32 pores, removal efficiency for large particles (>50 μm) remains comparable to the 8-pore configuration, whereas efficiency for fine inclusions (from 20 to 40 μm) decreases. This reduction correlates with flow-field disturbance induced by excessive pore density, which significantly alters the trajectories and deposition behaviors of fine inclusions, impairing their directional migration capability. Additionally, the data identify 50 μm as a critical particle size: below this threshold, pore number substantially influences removal efficiency, while above it, performance differences diminish across configurations. This confirms that removal of large inclusions is primarily governed by inertial transport and buoyancy-assisted flotation.

This study confirms through systematic experimental research and data analysis that employing an 8-pore structure with a 40° pore elevation angle in tundish filter configurations significantly enhances the comprehensive removal efficiency of non-metallic inclusions across the 20–80 μm size range. This optimized solution effectively balances filtration area and flow-field characteristics while ensuring molten-steel flow stability, achieving optimal removal efficiencies for inclusions of varying sizes.

3.2. Influence of Pore Number and Pore Elevation Angle on the Velocity Contour of Molten Steel in the Tundish

This study systematically investigates the influence mechanisms of tundish filters with varying pore numbers (from 2 to 32 pores) on molten-steel flow-field characteristics under 20–40°pore elevation angles through numerical simulation. As illustrated in Figure 9, the pore structure significantly affects the velocity-field distribution within the tundish, with Zone A and Zone B exhibiting differentiated evolutionary flow patterns as the pore number changes. Table 2 details the proportional variations of velocity color zones in Zone B across different pore numbers. Velocity contour maps and statistical flow-distribution data demonstrate substantial regulatory effects of pore configurations on steel-flow behavior. Quantitative results (Table 2) reveal pronounced flow nonuniformity in the 2-pore and

4-pore configurations: high-velocity zones (0.070–0.100 m/s) concentrate within limited pore channels, accounting for 25.58% and 6.18% of the area, respectively. Conversely, the 8-pore configuration achieves optimal flow characteristics with uniform velocity distribution (0.040–0.060 m/s), where medium and lower velocity zones constitute 52.23%. This ideal flow state ensures sufficient steel–filter contact while avoiding negative effects from velocity disparities.

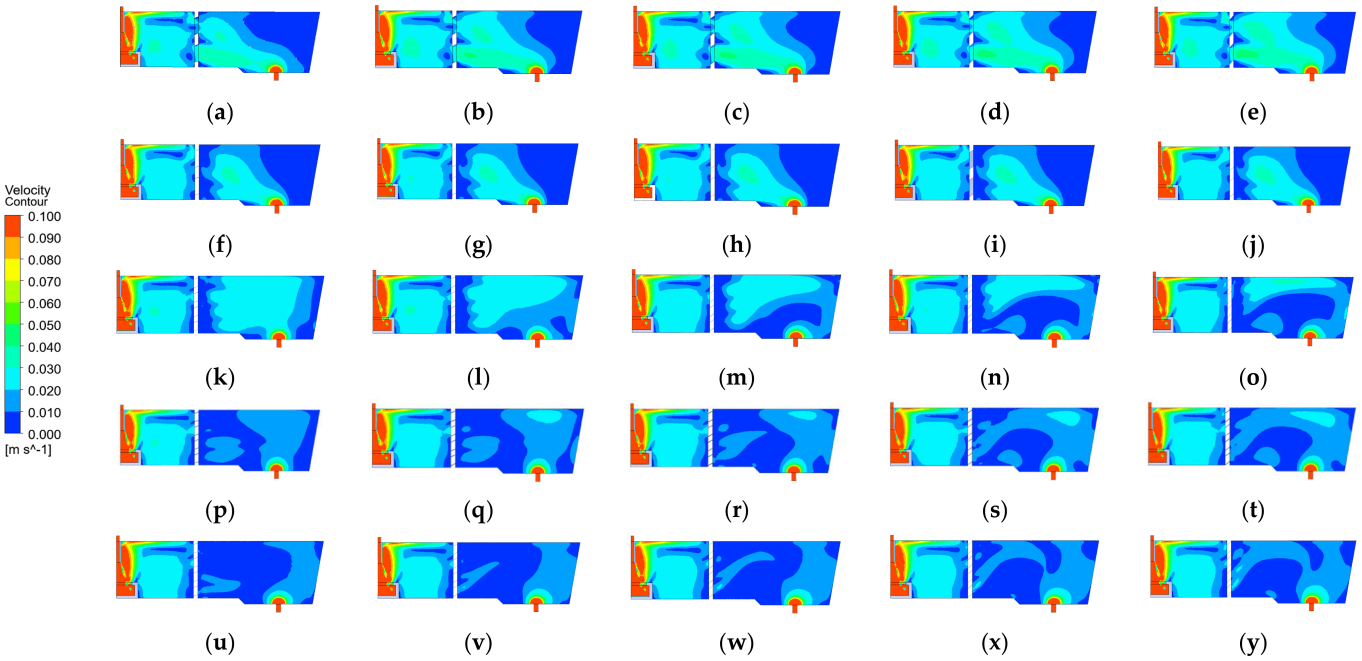


Figure 9. Influence of the pore number and pore elevation angle on the velocity contours of molten steel in the tundish filter (**a**–**y**). Rows from top to bottom represent filters with 2, 4, 8, 16, and 32 pores, respectively, and columns from left to right represent elevation angles of 20°, 25°, 30°, 35°, and 40°.

Table 2. Area fractions of different velocity zones in Zone B under different pore numbers at 40° pore elevation angle.

Pore Number	Green Proportion [%]	Bright Blue Proportion [%]	Light Blue Proportion [%]	Dark Blue Proportion [%]
2	25.58	25.73	23.42	23.84
4	6.18	24.01	24.34	44.85
8	2.40	17.06	35.17	44.70
16	0	6.09	55.20	37.01
32	0	3.93	49.78	45.98

When the pore number increases to 16 and 32 pores, low-velocity regions become dominant, high-velocity zones disappear completely, while lower and low-velocity regions exceed 80% coverage. This flow regime may prolong residence time excessively, potentially reducing filtration efficiency.

In-depth analysis identifies significant correlations between specific flow characteristics of the 8-pore filter at 40° (2.40% high velocity, 17.06% medium velocity, 35.17% lower velocity, 44.70% low velocity) and its optimal inclusion removal. This velocity profile achieves an ideal balance between turbulence intensity and residence time: moderate turbulence promotes the migration and capture of fine inclusions (20–40 μm), while appropriate residence behavior facilitates the removal of larger particles (>50 μm). Crucially, the 8-pore configuration avoids the excessive velocity gradients of the 2- and 4-pore designs and prevents the flow-separation phenomena observed in the 16- and 32-pore configurations.

This optimized flow structure provides hydrodynamic justification for its superior inclusion removal performance. The flow-field-density distribution across all pores at 40° further corroborates this observation, as presented in Table 2.

Integrating flow-field visualization and quantitative statistical results, this study clarifies the relationship among pore number, velocity distribution, and inclusion removal efficiency, elucidating the operational mechanism of tundish filters. The research confirms that the 8-pore and 40° configuration achieves optimal flow characteristics conducive to inclusion removal while maintaining sufficient filtration area.

3.3. Effect of Pore Number and Pore Elevation Angle on Molten-Steel Streamline Distribution

Figure 10 elucidates the regulatory mechanism of tundish filter pore structures on molten-steel flow characteristics under 20–40° elevation angles. Flow-field visualization analysis demonstrates significantly higher streamline density (indicating proportional steel distribution in specific zones) in Zone A than Zone B. Comparative analysis of flow fields across different pore numbers (2–32 pores) reveals a nonlinear relationship between pore number and streamline density (Table 3).

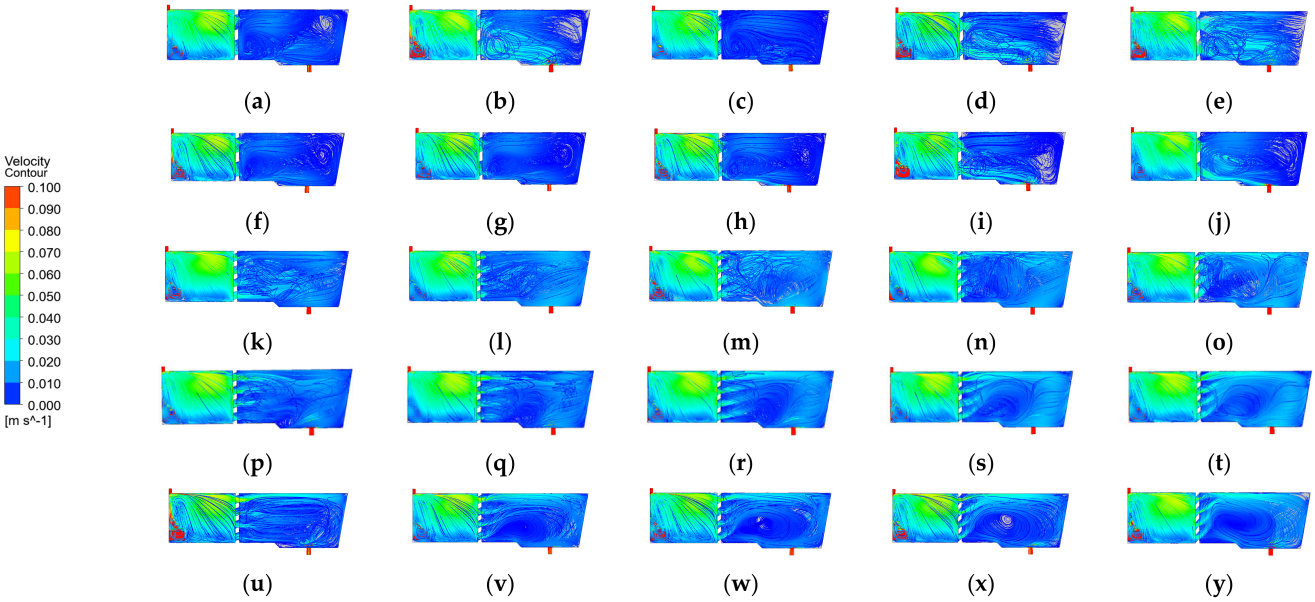


Figure 10. Influence of the pore number and pore elevation angle on flow diagram of molten steel in the tundish filter (**a**–**y**). Rows from top to bottom represent filters with 2, 4, 8, 16, and 32 pores, respectively, and columns from left to right represent elevation angles of 20°, 25°, 30°, 35°, and 40°.

Table 3. Streamline density of molten steel after passing through the filter.

Pore Number	Streamline Density of Molten Steel After Passing Through the Filter [%]
2	17.84
4	9.60
8	18.38
16	17.61
32	15.94

When comparing different pore-number configurations, the 8-pore filter exhibits the highest streamline density after molten steel passes through the filter, reaching 18.38%, followed by the 2-pore and 16-pore configurations, with values of 17.84% and 17.61%, respectively. This indicates that the 8-pore configuration provides better streamline cov-

erage and a higher probability of effective contact between molten steel, inclusions, and filter surfaces. The spatial distribution features of streamline density further explain the performance differences among the filter configurations. At low elevation angles of 20° to 30°, the 2-pore and 4-pore configurations exhibit localized streamline concentration, resulting in insufficient utilization of the effective filtration area. By contrast, although high-pore-number configurations provide more flow channels, the velocity contour maps reveal more dispersed and fragmented flow patterns, which may weaken the directional transport of inclusions toward the upper region of the tundish. The 8-pore configuration avoids the excessive flow concentration observed in low-pore-number filters while reducing the flow dispersion associated with the 16-pore and 32-pore filters. Therefore, it achieves a favorable balance between flow stability and filtration-area utilization. The non-monotonic variation in streamline density with pore number is mainly attributed to the competing effects of flow concentration and flow dispersion under the condition of constant total flow-through area. When the pore number is too low, molten steel tends to pass through a limited number of channels, leading to localized flow concentration and insufficient coverage of the effective filtration region. When the pore number is moderate, the flow distribution becomes more uniform while still maintaining sufficient directional transport, which is favorable for increasing streamline density. However, when the pore number becomes too high, the flow is excessively dispersed among many channels, weakening the overall flow coherence after passing through the filter. As a result, the streamline density does not increase monotonically with pore number, and an intermediate pore-number configuration exhibits the most favorable flow-distribution characteristics.

Further research demonstrates a significant positive correlation between inclusion removal efficiency and streamline density. The high streamline density (18.38%) of the 8-pore configuration corresponds to its optimal removal efficiency (74.33%), whereas the 16-pore and 32-pore configurations exhibit reduced removal efficiency of 74.05% and 73.44%, respectively, despite increased pore number, attributable to decreased streamline density. This phenomenon indicates a threshold effect in how pore number influences filtration performance: beyond 8 pores, increased pore density may expand contact area but flow dispersion weakens directional migration capability of inclusions. Flow-field analysis reveals that a relatively stable flow pattern with moderated velocity gradients formed by the 8-pore configuration balances turbulence intensity and residence time, simultaneously promoting the migration and capture of fine inclusions (20–40 μm) and inertial deposition of large particles (>50 μm), thereby achieving synergistic removal across the full particle size spectrum.

In summary, the 8-pore configuration significantly enhances filtration performance through synergistic optimization of pore structure and flow-field characteristics. Compared to the 4-pore configuration (streamline density: 9.60%, removal efficiency: 67.39%), it improves flow stability by 91.5% and increases removal efficiency by 10.3% at a 40° pore elevation angle. Moreover, its uniform streamline distribution prevents vortex generation, thus effectively preventing slag-entrainment risks. These outcomes provide a scientific basis for the structural design of filters in industrial applications.

3.4. Flow-Field Distribution at Filter Pores

To further clarify the flow-regulation mechanism of the tundish filter, the velocity distributions at the inlet and outlet cross-sections of the filter pores were analyzed. Compared with the global velocity contours and streamline distributions discussed above, the cross-sectional flow field of the filter pores provides more direct information on how molten steel enters, passes through, and exits the inclined channels. The turbulence inhibitor first redistributes the incoming molten-steel flow before it reaches the filter region, while the

filter pores further regulate the local flow direction and velocity distribution. Therefore, variations in pore number and pore elevation angle can directly affect the uniformity of the inlet flow, the stability of the outlet flow, and the subsequent migration behavior of inclusions. Based on this consideration, the velocity contours at the pore inlet and outlet were compared to evaluate the effect of filter geometry on local flow-field regulation and inclusion removal performance.

Figure 11 illustrates the influence of different pore numbers and pore elevation angles (20–40°) on velocity contour maps at the tundish filter inlet, with this study analyzing their effects on molten-steel velocity distribution across the inlet cross-section. Experimental results demonstrate that pore structure and pore elevation angle significantly regulate inlet flow characteristics: at any fixed elevation angle, the 2-pore and 4-pore configurations exhibit pronounced high-gradient velocity distributions featuring high-speed zones concentrated in narrow channels, indicating marked flow concentration. By contrast, the 8-pore configuration achieves optimal velocity uniformity, characterized by extensive isoline coverage and gentle gradients, reflecting superior flow stability. When the pore number increases to 16 and 32 pores, the overall inlet velocity decreases while the isoline distribution becomes fragmented, reducing flow uniformity. The study reveals that at a fixed pore number, smaller pore elevation angles generate discontinuous velocity fields and low-speed flows, whereas larger angles form continuous velocity fields with medium-high speeds. Medium-to-high-speed flows enable rapid inclusion flotation through the filter, facilitating sufficient contact with the top surface for effective absorption. This rapid-flotation mechanism significantly enhances inclusion removal efficiency. Conversely, discontinuous velocity fields and low-speed flows induced by smaller angles impede effective inclusion flotation.

Further analysis reveals consistent correlations between inlet-velocity-distribution characteristics and prior streamline density (Table 3) and inclusion removal efficiency (Table 1) data. The uniform inlet flow field of the 8-pore configuration corresponds to its highest streamline density (18.38%) and optimal removal efficiency (74.33%), demonstrating that inlet flow stability effectively enhances the penetration uniformity of molten steel within the filter. By contrast, concentrated high-speed flows in the 2–4-pore configurations may intensify localized turbulence, while dispersed low-velocity flows in the 16–32-pore configurations could impair inclusions migration efficiency. This correlation elucidates the governance mechanisms of pore number on filtration performance from a hydrodynamic perspective.

Figure 12 elucidates the influence of different pore numbers (2–32 pores) under varying pore elevation angles (20–40°) on molten-steel velocity distribution across the tundish filter outlet cross-section. Significant flow-field alterations occur after steel passes through the filter. Experimental data reveal that with the 2-pore and 4-pore configurations, the outlet velocity distribution exhibits distinct X-shaped asymmetry, characterized by lower central velocities and concentrated high-speed zones along both sides. This flow pattern may cause unbalanced percolation paths. Notably, the 16-pore and 32-pore configurations retain similar X-shaped distributions but demonstrate flattened velocity gradients. Conversely, the 8-pore configuration achieves ideal flow characteristics: uniform velocity distribution across the entire outlet cross-section without significant high-speed concentration or low-speed stagnation zones, indicating excellent flow stability during steel discharge. This flow pattern elucidates the threshold effect of pore number on filtration performance from outlet dynamics, confirming that the 8-pore structure optimizes outlet velocity distribution to effectively reconcile the conflict between inlet flow concentration and outlet energy dissipation.

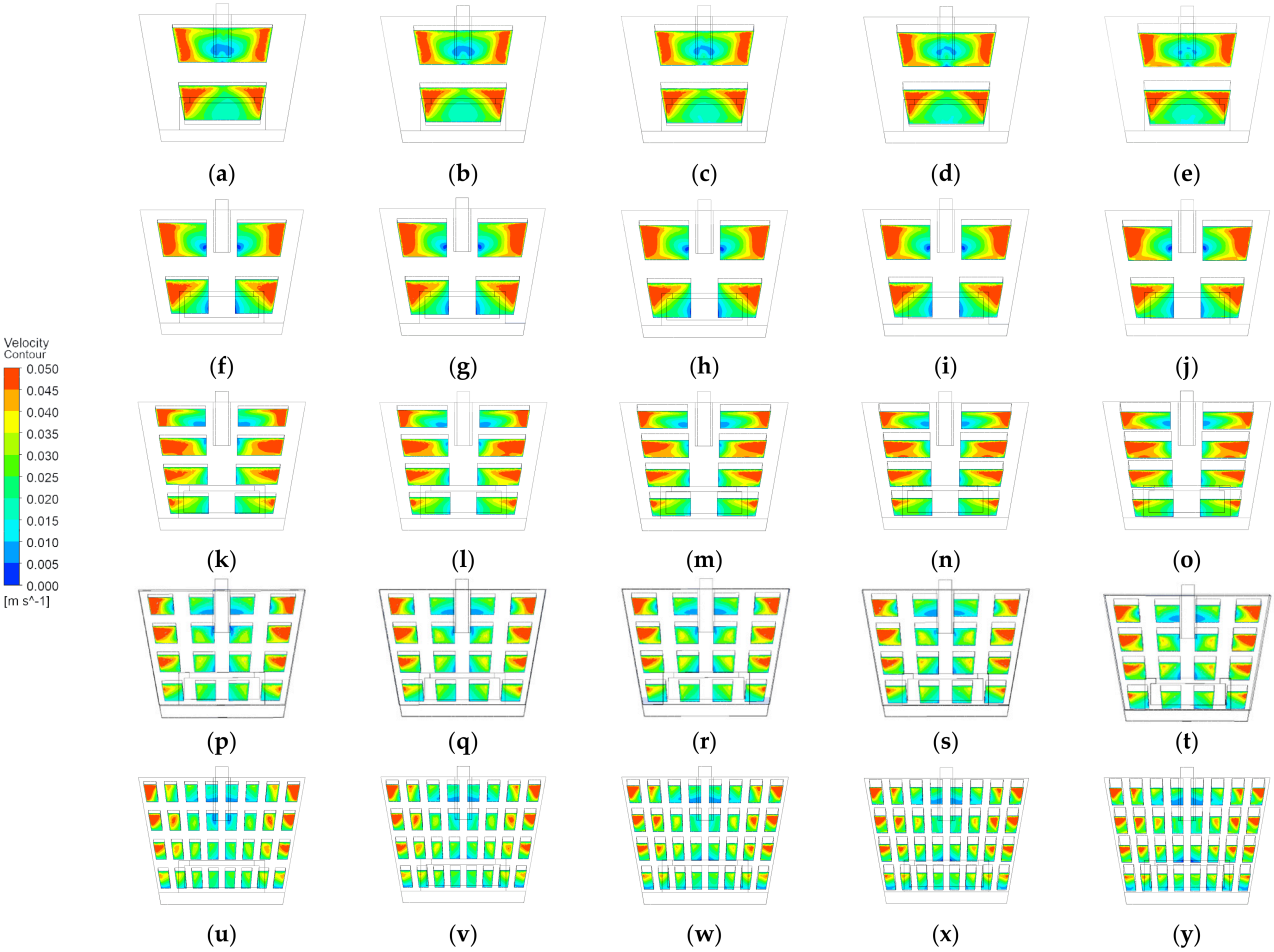


Figure 11. Influence of the pore number and pore elevation angle on molten-steel velocity contours at pore entrance of the tundish filter (**a**–**y**). Rows from top to bottom represent filters with 2, 4, 8, 16, and 32 pores, respectively, and columns from left to right represent elevation angles of 20°, 25°, 30°, 35°, and 40°.

In summary, the tundish filter with an 8-pore configuration and a 40° pore elevation angle achieves optimal balance between flow-field stability and inclusion removal efficiency by optimizing velocity distribution uniformity at both the inlet and outlet, while simultaneously reducing flow resistance. This finding provides a critical foundation for the structural design of tundish filters.

3.5. Vector Distribution of Tundish Filters

To further analyze the distribution characteristics of the molten-steel flow field, this study focuses on extracting high-density flow-field zones under different pore numbers and a 40° pore elevation angle and converting them into vector distributions, with relevant data detailed in Table 4.

Table 4. Vector density of molten steel at the pore outlet of the tundish filter.

Pore Number	Vector Density of Molten Steel at Pore Outlet of Tundish Filter [%]
2	11.55
4	11.40
8	15.60
16	21.60
32	13.50

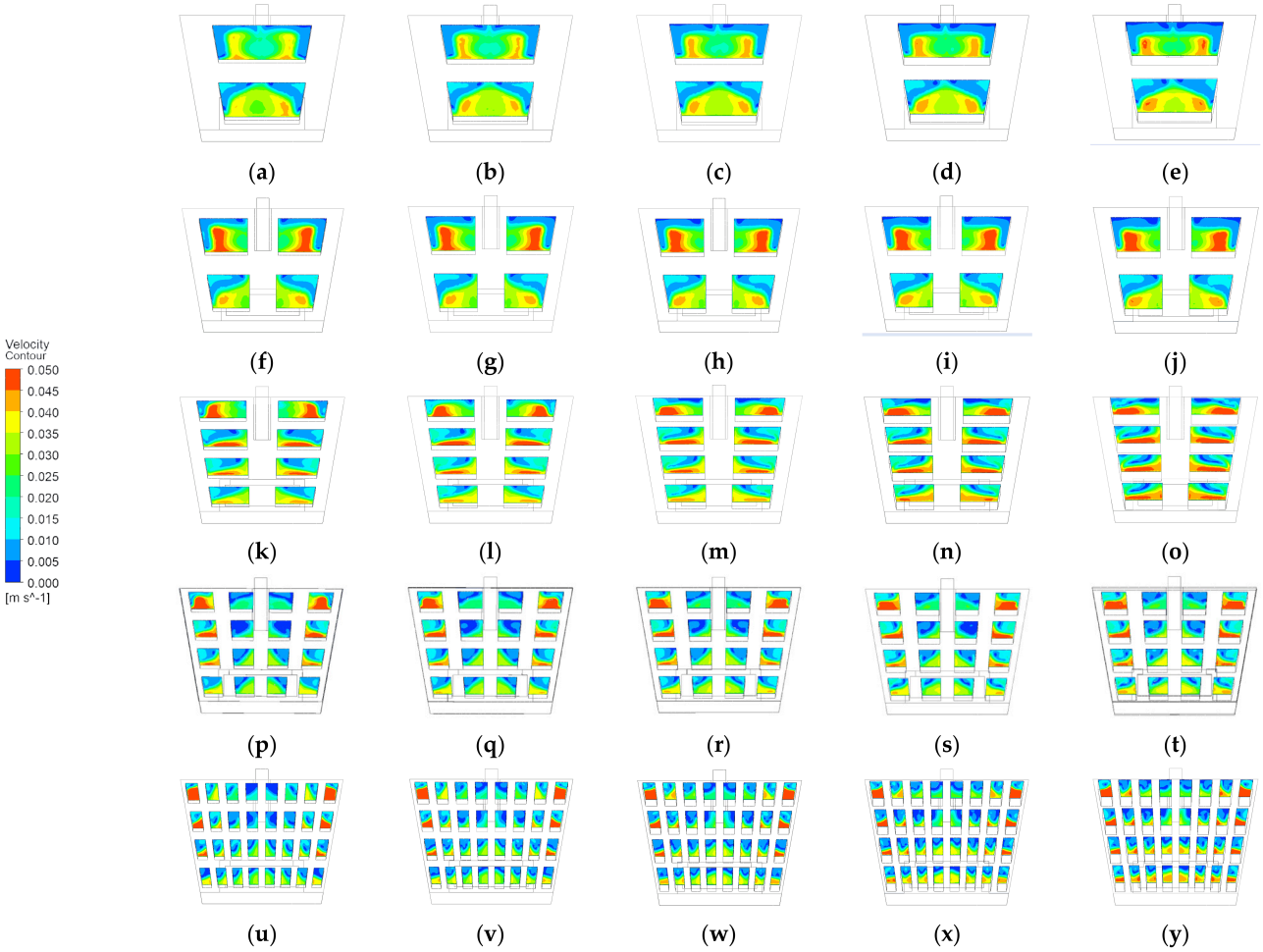


Figure 12. Influence of the pore number and pore elevation angle on molten-steel velocity contours at pore outlet of the tundish filter (**a**–**y**). Rows from top to bottom represent filters with 2, 4, 8, 16, and 32 pores, respectively, and columns from left to right represent elevation angles of 20°, 25°, 30°, 35°, and 40°.

Figures 13 and 14 elucidate the influence of different pore numbers on the flow-field characteristics at the tundish filter outlet. Experimental results demonstrate that pore structure significantly regulates vector distribution patterns of outlet flow. Under the 2-pore and 4-pore configurations (Figure 13a,b), vector directions exhibit localized concentration, with vector densities of 11.55% and 11.40%, respectively, indicating relatively singular and uneven flow paths. The 8-pore configuration (Figure 13c) increases vector density to 15.60%, displaying uniform vector distribution and consistent directional alignment, which reflects a stable and directionally coherent flow pattern during steel discharge. When the pore number reaches 16 pores, the vector density peaks at 21.60%. However, its vector diagram (Figure 13d) reveals localized vector dispersion, indicating potential flow separation or vortex generation. The 32-pore configuration shows decreased vector density (13.50%, Figure 13e) with further dispersed distribution, demonstrating that excessive pore number causes flow-field disturbance.

Further analysis reveals a nonlinear correlation between vector density and flow stability. Although the 16-pore configuration achieves the highest vector density, its flow uniformity decreases due to local vortices, consistent with prior findings showing that its removal efficiency is slightly lower than that of the 8-pore configuration. By contrast, the 8-pore configuration maintains a moderate pore number to achieve uniform vector distribution while sustaining a high vector density (15.60%), thereby optimizing the direc-

tional migration trajectories of inclusions. These results elucidate the threshold effect of pore number on filtration performance from a hydrodynamic perspective: excessive pore number (e.g., 16 pores and above) may increase flow path density but impairs filtration efficiency due to flow-field disturbance.

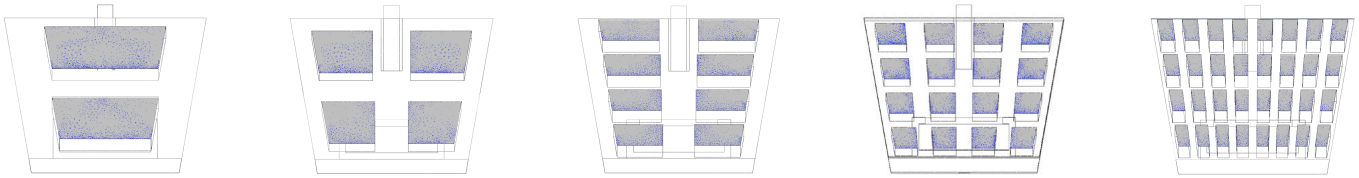


Figure 13. Influence of the pore number and pore elevation angle on the molten-steel vector diagram at the pore outlet of the tundish filter: (**a**) 2 pores, (**b**) 4 pores, (**c**) 8 pores, (**d**) 16 pores, (**e**) 32 pores.

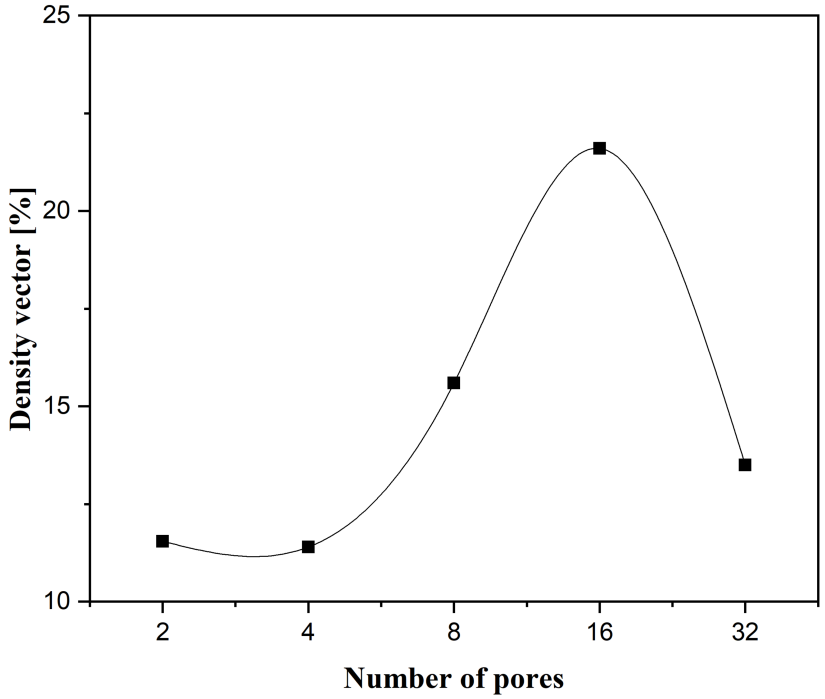


Figure 14. The relationship between the pore number with the same pore elevation angle and the topmost vector density at the filter outlet.

Comprehensive research demonstrates that the 8-pore and 40° configuration establishes a relatively stable and uniform outlet flow pattern by balancing vector density and flow distribution control. This simultaneously avoids the flow concentration issues inherent in the 2-pore and 4-pore configurations while overcoming the flow-dispersion defects observed in the 16-pore and 32-pore designs.

3.6. Mesh Sensitivity Test

To verify the reliability of the numerical results, a mesh sensitivity test was conducted using three mesh schemes, with approximately 0.8, 1.5, and 2.3 million cells, respectively. The 8-pore filter with a 40° pore elevation angle was selected as the representative case because it was the key optimized configuration in this study. The inclusion removal efficiencies obtained using the coarse, medium, and fine meshes were 71.29%, 74.33%, and 75.10%, respectively, as shown in Table 5.

Table 5. Effect of mesh resolution on inclusion removal efficiency and computational time.

Mesh Scheme	Cells (Million)	Inclusion Removal Efficiency [%]	Times [s]
Coarse mesh	0.8	71.29	47.38
Medium mesh	1.5	74.33	73.43
Fine mesh	2.3	75.10	122.76

The difference in inclusion removal efficiency between the medium and fine meshes was 0.77 percentage points, indicating that further mesh refinement had only a limited influence on the predicted removal efficiency. By contrast, the difference between the coarse and medium meshes was 3.04 percentage points, suggesting that the coarse mesh was insufficient for resolving the local flow field near the filter channels. Therefore, the medium mesh with approximately 1.5 million cells was adopted in the subsequent simulations, as it provided a suitable balance between computational accuracy and efficiency. The computational time also increased with mesh refinement, further supporting the use of the medium mesh for the full set of 25 simulation cases. In addition, the predicted tendencies in the present study are qualitatively consistent with previously published results on tundish filters and multi-hole porous structures [28,29], which further supports the reliability of the numerical analysis.

3.7. Metallurgical Performance Improvement of the Optimized Filter Configuration

The metallurgical performance improvement achieved using the optimized tundish filter is mainly reflected in the coordinated enhancement of flow regulation and non-metallic inclusion removal. Compared with low-pore-number configurations, the filter with 8 pores and a 40° pore elevation angle reduced local flow concentration and produced a more uniform and stable flow pattern. Compared with high-pore-number configurations, it avoided excessive flow dispersion and maintained effective directional transport of molten steel after passing through the filter. As a result, this configuration provided more favorable hydrodynamic conditions for the upward migration and capture of inclusions at the slag/flux layer and filter surfaces, leading to the highest average inclusion removal efficiency among all simulated cases. Therefore, the optimized filter structure exhibited improved metallurgical performance in terms of tundish flow control and steel-cleanliness enhancement.

4. Conclusions

This study systematically evaluated the influence of pore number and pore elevation angle in tundish filters on molten-steel flow behavior and non-metallic inclusion removal. The results demonstrated that the filter with 8 pores and a 40° pore elevation angle achieved the optimal performance, with an average inclusion removal efficiency of 74.33% for inclusions in the size range of 20 to 80 μm. This configuration effectively balanced flow uniformity and stability by mitigating localized flow concentration in low-pore-number filters and avoiding excessive flow dispersion in high-pore-number filters. Consequently, a more favorable flow field was established for the upward transport of inclusions and their capture at the slag/flux layer and filter surfaces. These results indicate that the coordinated optimization of pore number and pore elevation angle is an effective approach for improving the metallurgical performance of tundish filters and provides a quantitative basis for the structural design of flow-control devices in continuous casting tundishes. From a practical perspective, the optimized filter configuration may contribute to improved steel cleanliness, more stable tundish flow control, and reduced risks associated with inclusion-related defects, thereby providing potential technological and economic benefits for continuous casting operations. Future work should validate the present numerical

predictions through physical modeling and industrial trials and should further evaluate the effects of thermal conditions, operating fluctuations, refractory wear, and manufacturing feasibility on the practical implementation of the proposed filter configuration.

Author Contributions: Conceptualization, A.L.; Methodology, D.F. and S.L.; Software, S.L.; Validation, D.Q.; Formal analysis, A.L.; Investigation, D.F.; Resources, J.Y.; Data curation, D.Q.; Writing—original draft, A.L.; Writing—review & editing, D.F. and X.L.; Visualization, J.Y.; Supervision, D.Q.; Project administration, A.L.; Funding acquisition, X.L. All authors have read and agreed to the published version of the manuscript.

Funding: This work was supported by the Liaoning Province Science and Technology Plan Joint Plan Project (2025-BSLH-182), the Key Project of Liaoning Public Welfare Research Fund for Science (2025JH4/10100011), and the Liaoning Provincial Department of Education University Basic Research Project (L232510146001).

Data Availability Statement: The original contributions presented in this study are included in the article. Further inquiries can be directed to the corresponding authors.

Conflicts of Interest: The authors declare no conflicts of interest.

Nomenclature

Symbol/Abbreviation	Description
CFD	Computational fluid dynamics
DPM	Discrete phase model
k	Turbulent kinetic energy [m^2/s^2]
ε	Turbulent dissipation rate [m^2/s^3]
ρ, ρ_p	Molten-steel density and particle density [kg/m^3]
t	Flow time [s]
x, y, z, x_i, x_j	Coordinate directions [m]
v_x, v_y, v_z, u_i, u_j	Velocity components of molten steel [m/s]
u, u_p	Molten-steel velocity and inclusion-particle velocity [m/s]
P	Pressure [Pa]
μ, μ_{eff}	Dynamic viscosity and effective viscosity [kg/(m·s), Pa·s]
g, g_i	Gravitational acceleration and its component [m/s^2]
F_D	Drag term coefficient [s^{-1}]
F_x	Additional force term per unit particle mass [m/s^2]
d_p	Inclusion-particle diameter [m]
C_D, Re	Drag coefficient and particle Reynolds number

References

1. Lin, P.; Jin, Y.; Gan, F.; Ma, G.; Cheng, C.; Huang, Z.; Ling, H. Research on Turbulence Inhibitor Strengthening in Fluid–Thermal–Stress Coupling Modes for a Tundish. *Metall. Mater. Trans. B Process Metall. Mater. Process. Sci.* **2025**, *56*, 1728–1743. [CrossRef]
2. Liu, Y.; Chu, R.; Li, X.; Hao, N.; Wang, W. Simulation of the effect of continuous casting tundish filter on removing inclusions in steel. In Proceedings of the 12th Global Conference on Materials Science and Engineering, CMSE 2023, Shenzhen, China, 27–30 October 2023.
3. Wang, X.; Hu, H.; Shi, P.; Xie, X.; Wu, C.; Chen, D.; Long, M. Optimization of Deflector Hole on Porous Baffle Wall in Six-Strand Tundish for Bloom Continuous Casting. In Proceedings of the Materials Processing Fundamentals Symposium held at the TMS Annual Meeting and Exhibition, Orlando, FL, USA, 3–7 March 2024; pp. 281–291.
4. Qin, X.-F.; Cheng, C.-G.; Li, Y.; Wu, W.-L.; Chen, H.; Zhao, C.-F.; Jin, Y. Numerical simulation on gas–liquid multiphase flow behavior under coupling effects of annular gas curtain and swirling flow at tundish upper nozzle. *J. Iron Steel Res. Int.* **2024**, *31*, 2693–2709. [CrossRef]

5. Wang, J.; Liu, Z.; Chen, W.; Chen, H.; Zhang, L. Numerical simulation on the multiphase flow and reoxidation of the molten steel in a two-strand tundish during ladle change. *Int. J. Miner. Metall. Mater.* **2024**, *31*, 1540–1553. [CrossRef]
6. Zhou, Y.; Zou, X.; Ma, Z.; Wu, C.; Li, Y. Numerical Simulation Study of a Pusher Feed Classifier Based on RNG-DPM Method. *Processes* **2024**, *12*, 1151. [CrossRef]
7. Qin, X.; Cheng, C.; Chen, H.; Li, Y.; Jin, Y. Numerical Study on Metallurgical Effect of Filtering Weir with Multi-stepped Orifices in Tundish. *Metall. Mater. Trans. B Process Metall. Mater. Process. Sci.* **2024**, *55*, 1910–1924. [CrossRef]
8. Zhang, Z.-X.; Wang, H.; Qu, T.-P.; Wang, D.-Y.; Li, X.-L.; Hu, S.-Y.; Tian, J.; Zhou, X.-Z.; Yang, Z.-H. Numerical Investigation on Transient Flow and Inclusion Removal Behavior in Tundish During Ladle Change Process. *Steel Res. Int.* **2024**, *95*, 2400471. [CrossRef]
9. Neumann, S.; Asad, A.; Schwarze, R. Numerical Simulation of an Industrial-Scale Prototypical Steel Melt Tundish Considering Flow Control and Cleaning Strategies. *Adv. Eng. Mater.* **2020**, *22*, 1900658. [CrossRef]
10. Xing, F.; Zheng, S.; Zhu, M. Channel parameter optimization of one-strand slab induction heating tundish with double channels. *High Temp. Mater. Process.* **2024**, *43*, 20220312. [CrossRef]
11. Wang, Z.; Li, Y.; Wang, X.; Li, X.; Yue, Q.; Xiao, H. Channel-Type Induction Heating Tundish Technology for Continuous Casting: A Review. *Materials* **2023**, *16*, 493. [CrossRef] [PubMed]
12. Demeter, P.; Buko, B.; Dzurak, R.; Priesol, I.; Hubatka, S.; Fogara, L.; Hrubovakova, M.; Demeter, J. The Development of an Optimized Impact Pad for a Six-Strand Tundish Using CFD Simulations. *Appl. Sci.* **2025**, *15*, 5450. [CrossRef]
13. Song, J.; Chen, C.; Guo, Z.; Geng, M.; Rong, Z.; Wang, T.; Wang, J.; Dianyu, E.; Fan, J.; Sun, Y. Analysis of Flow Field, Temperature, and Inclusion Evolution in a 12-Strand Tundish During Ladle Changeover Process. *Metall. Mater. Trans. B Process Metall. Mater. Process. Sci.* **2025**, *56*, 2700–2714. [CrossRef]
14. Wang, T.F.; Chen, W.C.; Hsu, W.Y.; Huang, C.C.; Fukui, K.; Huang, A.N.; Kuo, H.P. Approaching particle deposition separation characteristics in the Empty Nose Syndrome (ENS) nasal cavities with CT image-based nasal cavity and CFD-DPM simulations. *Powder Technol.* **2025**, *458*, 120954. [CrossRef]
15. Zhao, D.; Liu, A.; Qiu, S.; Lai, C. Physical and Mathematical Simulation of Molten Steel Flow Field in Tundish with Filter. *Spec. Steel* **2016**, *52*, 5.
16. Yan, J.; Xiaosen, D.; Fu, Y.; Changgui, C.; Yang, L.; Wei, W. Removal Mechanism of Microscale Non-Metallic Inclusions in a Tundish with Multi-Hole-Double-Baffles. *Metals* **2018**, *8*, 611. [CrossRef]
17. Quintero-Payan, A.C.; Huete-Hernandez, S.; Aguilar-Pozo, V.B.; Astals, S.; Chimenos, J.M. Stabilization of metal and metalloids from contaminated soils using magnesia-based tundish deskulling waste from continuous steel casting. *Chemosphere* **2024**, *348*, 140750. [CrossRef]
18. Yang, B.; Liu, K.; Lei, H.; Han, P. Structure optimization of continuous casting tundish with channel-type induction heating using mathematical modeling. *High Temp. Mater. Process.* **2022**, *41*, 460–468. [CrossRef]
19. Wang, J.; Liu, W.; Yang, S.; Zuo, X.; Zhao, L.; Li, J. Effect of Tundish Impact Zone Optimization on Inclusion Removal in Steel: Industrial and Simulation Studies. *Metall. Mater. Trans. B Process Metall. Mater. Process. Sci.* **2024**, *55*, 808–820. [CrossRef]
20. Hu, W.; Wang, Y.; Pei, P.; Li, C.; Huang, S.; Bao, W.; Zhou, J. Heat transfer characteristics and stress analysis of a new tundish with vacuum chambers. *Appl. Therm. Eng.* **2024**, *247*, 123065. [CrossRef]
21. Qin, B.; Zhang, J.; Yang, C.; Yang, S.; Liu, Q. Study on Influencing Factors and Their Combined Effects on Multiphase Behavior in Tundish Pouring Zone. *Metall. Mater. Trans. B Process Metall. Mater. Process. Sci.* **2025**, *56*, 1176–1191. [CrossRef]
22. Najera-Bastida, A.; Morales, R.D.; Guarneros-Guarneros, J.; Rodriguez-avila, J.; Solis-Marcial, O.J. Effect of the Tundish Inhibitor Design on the Flotation Efficiency of Nonmetallic Inclusions: Water Modeling and Mathematical Simulations by the Reynolds Stress Model. *Steel Res. Int.* **2024**, *95*, 2400087. [CrossRef]
23. Zhao, X.-Y.; Zhang, J.-M.; Wu, S.-Z.; Hu, B. Transient simulation on the behavior of inclusions in liquid steel of the tundish with a filter. *Beijing Keji Daxue Xuebao/J. Univ. Sci. Technol. Beijing* **2011**, *33*, 539–543.
24. Sahai, Y. Tundish Technology for Casting Clean Steel: A Review. *Metall. Mater. Trans. B* **2016**, *47*, 2095–2106. [CrossRef]
25. Wang, X.-Y.; Zhao, D.-T.; Qiu, S.-T.; Zou, Z.-S. Effect of tunnel filters on flow characteristics in an eight-strand tundish. *ISIJ Int.* **2017**, *57*, 1990–1999. [CrossRef]
26. Bartosiewicz, M.; Cwudziski, A. Influence of multi-hole filter modification on the flow hydrodynamic structure and refining process of liquid steel in the one-strand Tundish. *Arch. Metall. Mater.* **2019**, *64*, 71–78. [CrossRef]
27. Wang, J.; Liu, Y.; Xie, X.; Fang, Q.; Wang, J.; Wang, G.; Zhang, H. A comprehensive assessment of metallurgical effect of gas curtain on a two-strand tundish. *ISIJ Int.* **2025**, *65*, 1441–1453. [CrossRef]

28. Liu, C.; Xiao, A.; He, Z.; Yan, W.; Li, G.; Wang, Q. Numerical Investigation on Motion and Removal of Inclusions in Continuous Casting Tundish with Multiorifice Filter. *Steel Res. Int.* **2022**, *93*, 2100818. [CrossRef]
29. Wang, Q.; Liu, Y.; Huang, A.; Yan, W.; Gu, H.; Li, G. CFD Investigation of Effect of Multi-hole Ceramic Filter on Inclusion Removal in a Two-Strand Tundish. *Metall. Mater. Trans. B Process Metall. Mater. Process. Sci.* **2020**, *51*, 276–292. [CrossRef]

Disclaimer/Publisher's Note: The statements, opinions and data contained in all publications are solely those of the individual author(s) and contributor(s) and not of MDPI and/or the editor(s). MDPI and/or the editor(s) disclaim responsibility for any injury to people or property resulting from any ideas, methods, instructions or products referred to in the content.